Electronics Testing, LArSoft Analysis, and Data Acquisition for MicroBooNE

Victor Genty*
Columbia University, Nevis Laboratories, Irvington, New York†
(Dated: August 2, 2013)

This paper presents a variety of projects completed for the neutrino group at Nevis Labs. MicroBooNE electronics are tested including gain of phototubes, and a study of splitter reflection between the phototube, signal shaper. LArSoft analysis is presented for cluster reconstruction algorithms on whole detector simulation. Two clustering algorithms are compared. Visible energy reconstruction is also studied. Data acquisition software and hardware for photomultipliers are calibrated for the MicroBooNE optical system.

I. INTRODUCTION

A. The Standard Model

The Standard Model of elementary particles and their interactions is a quantum field theory of the electromagnetic, weak, and strong nuclear forces. Certified by its remarkable success at describing a diverse body of experimental observation, the standard model is one of the most successful theories in physics today. According to this model, all of matter is constructed of 12 spin-1/2 particles known as fermions: six *leptons* and six *quarks* [1].

Quarks carry fractional charges $+\frac{2}{3}$ and $-\frac{1}{3}$, and are grouped according to flavor: 'up', 'down', 'charm', 'strange', 'top', and 'bottom'. Participating the electromagnetic, weak, strong interactions, quarks are bound together forming hadronic matter: mesons and baryons. Quarks only exist in bound states, and therefore are not directly observable.

Increasing in mass to the right, Leptons are integer charged and interact via the electromagnetic and weak forces. The most familiar particle is the electron, e^-. The two heavier leptons are called the muon, μ, and tau, τ. The particles in the bottom lepton row are called neutrinos and have unknown, but small non-zero mass.

Each force in the Standard Model has associated with it a set of spin 1 carrier particles. The electromagnetic force is mediated by exchange of photons, γ, the weak mediated by $W^{\pm}$ and Z particles, and the strong interaction by a set of 8 particles called gluons, g.

The Higgs mechanism is responsible for giving mass to the fundamental fermions through spontaneous symmetry breaking [2]. The Higgs particle is a scalar boson with neither color nor electric charge.

Through a description of 12 fundamental particles and three forces, the Standard Model predicts the richness of particle dynamics, a multitude of observed composite particles, anti-particles, and much more [3].

Particle	Flavor			Q/e
leptons	e	μ	τ	-1
	ν_e	ν_μ	ν_τ	0
quarks	u	c	t	$+\frac{2}{3}$
	d	s	b	$-\frac{1}{3}$

TABLE I: The fundamental fermions of the Standard Model: particle names, flavor, and ratio of electric to fundamental charge.

B. Neutrino Oscillations

In the Standard Model neutrinos are assumed massless and only interact via the weak force. Massive neutrinos were first studied by Italian physicist Bruno Pontecorvo in the 1950s as an analogy to neutral kaon mixing [4]. According to the theory, neutrinos are created and annihilated as *flavor* eigenstates: ν_e, ν_μ, ν_τ but propagate through space in so called *mass* eigenstates: ν_1, ν_2, ν_3. Each flavor eigenstate can be expressed as a linear combination of mass eigenstates,

$$|\nu_\alpha\rangle = \sum_i U_{\alpha i}|\nu_i\rangle,$$

according to a unitary 3×3 mixing matrix,

$$U = \begin{pmatrix} U_{e1} & U_{e2} & U_{e3} \\ U_{\mu 1} & U_{\mu 2} & U_{\mu 3} \\ U_{\tau 1} & U_{\tau 2} & U_{\tau 3} \end{pmatrix},$$

for $|\nu_\alpha\rangle$ a neutrino of definite flavor with $\alpha \in [e, \mu, \tau]$ and $|\nu_i\rangle$ a neutrino of definite mass with $i \in [1, 2, 3]$. $U_{\alpha i}$ is the so called Pontecorvo-Make-Nakagawa-Sakata (PMNS) matrix analogous to the Cabbibo-Kobayashi-Masakawa (CKM) matrix of quark mixing. The matrix can be decomposed into four mixing matrices between the eigenstates:

$$U = \begin{pmatrix} 1 & 0 & 0 \\ 0 & c_{23} & s_{23} \\ 0 & -s_{23} & c_{23} \end{pmatrix} \begin{pmatrix} c_{13} & 0 & s_{13}e^{-i\delta} \\ 0 & 1 & 0 \\ -s_{13}e^{i\delta} & 0 & c_{13} \end{pmatrix} \begin{pmatrix} c_{12} & s_{12} & 0 \\ -s_{12} & c_{12} & 0 \\ 0 & 0 & 1 \end{pmatrix},$$

*Electronic address: vic.genty@gmail.com
†Permanent address: The University of Texas at Austin, Department of Physics, Austin, Texas

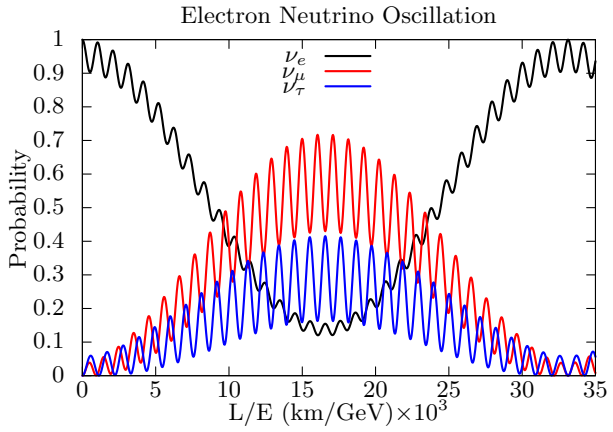

FIG. 1: Vacuum oscillation probability for an initial electron flavor state. The PDG values $\sin^2 2\theta_{12} = 0.857$, $\sin^2 2\theta_{23} = 0.95$, $\sin^2 2\theta_{13} = 0.095$, $\Delta m^2_{32} = 2.32 \times 10^{-3}\text{eV}^2$, $\Delta m^2_{21} = 0.75 \times 10^{-5}\text{eV}^2$, and $\delta = 0$ are used [4].

where $c_{ij} = \cos\theta_{ij}$ and $s_{ij} = \sin\theta_{ij}$. The angles θ_{ij} parameterize the relationship between flavor and mass eigenstates. The phase δ is only non zero, i.e. $U^* = U$, if neutrinos violate charge-conjugate and parity (CP) symmetry. Assuming massive neutrino propagating plane waves of the form,

$$|\nu_i(t)\rangle = e^{-i(E_i t - \mathbf{p}\cdot\mathbf{r})}|\nu_i(0)\rangle,$$

for the energy of a mass eigenstate $E_i = \sqrt{|\mathbf{p}|^2 + m_i^2}$, t time, $\mathbf{p}$ the 3-momentum, and $\mathbf{r}$ the neutrino position, the oscillation probability between two flavor states α and β is their inner product in time,

$$P(\nu_\alpha \to \nu_\beta) = |\langle\nu_\beta|\nu_\alpha\rangle|^2 = \left|\sum_i U^*_{\alpha i} U_{\beta i} e^{-i m_i^2 L/2E}\right|^2,$$

assuming ultra relativistic neutrinos. In the two neutrino model described by a 2×2 mixing matrix the oscillation probability simplifies to

$$P(\nu_\alpha \to \nu_\beta) = \sin^2 2\theta \ \sin^2(1.27\Delta m^2 L/E).$$

For L the distance from the flavor eigenstate creation and E its energy. The above equation demonstrates that neutrino flavors oscillate in time, or distance traveled, and are dependent on mixing angle, energy, and their squared mass difference. It is the job of experimentalist to measure these parameters.

In FIG 1 shown above, an electron neutrino oscillation probability to muon and tau flavor neutrinos varies as a function of the ratio of propagation distance to energy. The presence of three neutrino mixing produces small oscillations overlayed on a larger periodic behavior. Experimentally measured parameters are used from the Particle Data Group (PDG) assuming normal mass hierarchy.

Neutrino oscillations are a precise method for studying quantum coherence between weak flavor states. Unfortunately, oscillation experiments are only sensitive to differences in neutrino masses and not absolute mass. In addition, the mass hierarchy of neutrino mass states are currently unknown.

C. Neutrino Detection

Neutrinos and their oscillation parameters are the focus of an intense experimental interest in recent years. Due to the nature of the weak interaction, neutrino detection is difficult. Experiments must receive and collect a large flux of neutrinos to detect only a few number of events. Neutrinos are typically detected through process such as inverse beta decay, or charged and neutral current interactions with hadrons. Modern experiments use a combination of scintillation or cherenkov radiation and calorimetry coupled to photomultiplier tubes to detect and track neutrino interactions. Many experiments utilize novel techniques such as time projection chambers. Experimental detection of neutrinos can be grouped into four categories: solar, atmospheric, reactor, and beam neutrino detection.

The oldest and first experimental detection of neutrino oscillations came from evidence of deficits in neutrino rates produced in fusion products from the Sun. The Homestake experiment in Lead, South Dakota measured only one-third of theoretical calculations for the electron anti-neutrino flux from the Sun [6]. The experimenters used the process of inverse beta decay between chlorine and argon to count the solar neutrino production rate. A more modern experiment called SNO (Sudbury Neutrino Observatory) carried 1,000 tonnes of deuterium oxide in a spherical vessel. SNO measured charged and neutral current interactions [7] for electron neutrino interactions. Solar neutrino experiments are particularly sensitive to θ_{12} and Δm^2_{12} oscillation parameters.

Atmospheric oscillation experiments measure neutrinos and anti-neutrinos produced in high energy cosmic ray decays in Earth's upper atmosphere. Neutrinos created from charged pion and muon decay products are studied. Precise experimental evidence for atmospheric neutrino oscillation was first discovered in 1998 by the SuperKamiokande experiment which used a giant water detector to measure atmospheric neutrinos. Atmospheric detection experiments are sensitive to θ_{23} and Δm^2_{23} parameters.

Reactor experiments utilize anti-neutrinos produced in fission reactors and measure their disappearance over distance. Nearly all reactor experiments including Double Chooz, Daya Bay, and Reno, implement an identical near and far detector to count neutrino disappearance. The experiments involve liquid scintillator and photomultiplier tubes surrounded by a veto region to measure inverse beta decay events. Typically, the liquid scintillator is doped with a rare-earth metal to en chance neutron

capture rates. Rector experiments are sensitive to θ_{13} and currently have set the best limits on the value.

Lastly, neutrino beam experiments employ particle accelerators to create a defined neutrino flux and measure neutrino appearance. Experiments such as MINOS, T2K, NOνA are a few of the long-baseline schemes to detect neutrinos produced when high energy proton beams impinge on a target. The pions and kaons produced from strong interactions with the target decay in flight to muon and electron neutrinos. It is the goal of beam experiments to measure θ_{23}, and Δm^2_{23} values.

Each neutrino source and detection method is sensitive to the different neutrino oscillation parameters in the PMNS matrix. Other notable experiments such as NEMO-3 measuring neutrinoless double beta decay, and IceCube measuring high energy astophysical neutrinos, provide important insight into less studied area of contemporary neutrino physics.

II. MICROBOONE

A. History

In 1995 and 1996, the Liquid Scintillator Neutrino Detector (LSND) experiment at Los Alamos reported evidence for $\bar{\nu}_\mu \rightarrow \bar{\nu}_e$ oscillations. A low energy *excess*, $\sim 3.8\sigma$ [8], of $\bar{\nu}_e$ events in a pure $\bar{\nu}_\mu$ beam was found. The allowed values of Δm^2 and $\sin^2 2\theta$ measured from the experiment were in conflict with standard model oscillation theory. High Δm^2 values were not excluded from the data analysis. The LSND result could also not be explained by atmospheric or solar oscillations as they required too low of Δm^2 values. The LSND experiment suggested the presence of a fourth neutrino with a large mass splitting compared to the three known flavors. One method to accommodate additional mass splittings in the neutrino sector is the introduction of so called "sterile neutrinos" which act as new flavors that mix with the known Standard Model flavors. To avoid the limits on the active neutrinos, sterile neutrinos would not couple to the W or Z bosons [5]. The MiniBooNE experiment was the first attempt to verify LSND's observation. The MiniBooNE detector is an oil-based cherenkov radiation detector measuring neutrino oscillation from the Fermilab Booster beam. The Fermilab Booster is a 500 foot diameter, 8 GeV circular proton accelerator. MiniBooNE found an excess of not only $\bar{\nu}_e$ as in LSND, but in ν_e appearance as well from ν_μ and $\bar{\nu}_\mu$ beams. In addition, these results were measured at an even *lower* energy that from LSND. Unfortunately the evidence was not conclusive enough to declare the existence of sterile neutrinos but was able to rule out the two neutrino oscillation model [9]. The excess could have been oscillations, photon radiation, or ν background. To reconcile the observations of LSND and MiniBooNE, the MicoBooNE experiment was proposed.

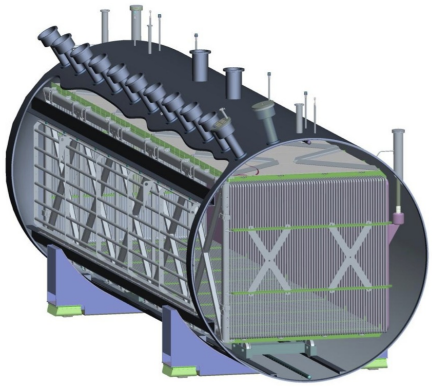

FIG. 2: MicroBooNE's liquid argon time projection chamber surrounded by the 170 ton liquid argon cryostat.

B. Motivation and Goals

The MicroBooNE experiment, located at Fermilab, is a beam neutrino experiment located along the Booster neutrino beam line. Motivated by the LSND and MicroBooNE low energy excess, MicroBoone will search for sterile neutrinos and hopefully elucidate the previous experiments results. What sets MicroBooNE apart from previous experiments is its high efficiency at reconstructing neutrino interactions, begin nearly free of particle misidentification background [9]. MicroBooNE improves on the MiniBooNE detector by being able to separate photon and electron signals in the time project camber. This background was a significant source of uncertainty for the MiniBooNE device.

One of MicroBooNE's secondary goals is be sensitive to cosmic neutrino flux if a Super Nova event were to occur. The detector will be operating continuously around the clock and along will real time astronomical data will be able to trigger data read out to possibly collect neutrinos from such an event.

MicroBooNE will also serve as a physics research and development for future long baseline neutrino experiments such as the Long Baseline Neutrino Experiment (LBNE) which are projected to definitively test for CP violation in the neutrino sector.

C. Detector

MicroBooNE is currently being installed at a distance of 469 meters from the beryllium target at Fermilab. Shown in FIG. 2, MicroBooNEs 70 ton fiducial volume is within a $2.5\times2.4\times10.4$ meter^3 drift region of active liquid argon volume. The total mass of Argon in the detector is 170 tons. One of the most important aspects of the detector is the Liquid Argon Time Projection Chamber.

MicroBooNE's detection apparatus is a Liquid Argon Time Projection Chamber (TPC). TPC's are one of the most promising technologies for future large scale neu-

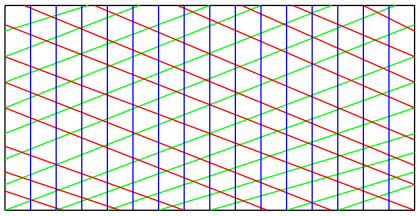

FIG. 3: Orientation of wire planes in MicroBooNE TPC chamber. The U (green), and V (red) are induction planes oriented at $+60^\circ$ and -60° with respect to the vertical, and Y (blue) is the collection plane. Electrons from ionization are collected on the collection plane only.

trino detectors [9]. The Booster proton beam will impinge on a Beryllium target and the resulting charged mesons are focused into a decay pipe. In the decay pipes, kaons and pions will decay and an absorber will filter the final states for neutrinos. The neutrinos pass through a region of dirt and will enter into the liquid argon chamber and interact via charged and neutral current interactions, ionizing Argon atoms. An electric field of 500 V/cm provided by a negatively charged cathode plate will drift ionization electrons onto three recording planes at a speed of 1.6 mm/μs. The recording planes are shown in FIG. 3. The electrons will drift a maximum distance of 2.5 meters past the negatively biased U, and V wire planes including voltage pulses. The wireplanes are separated by 3 mm. The electrons will be collected on the collection wires. Together with photomultiplier tubes the three wire planes, separated by 3 mm, will provided enhanced 3 dimensional reconstruction ability for the fiducial volume. The wire locations and electron arrival time on the wires enables sub-millimeter position resolution. In addition to the TPC, 30 photomultiplier tubes will be used to determine event timing from argon scintillation at 128 nm. Detector electronics will be able to select events in time with the Booster neutrino beam passage.

III. ELECTRONICS TESTING

A. PMT Gain Study

Photomultiplier tubes (PMTs) are electron tube devices which convert light into an electric current through the photoelectric effect. The PMTs to be used in the MicroBooNE detector are 8-inch Hamamatsu R5912-02mod. Photomultipliers in MicroBooNE will provide important event timing information for triggering on neutrino interactions, in addition to aiding in the separation of electron and photon signals. A secondary objective of the PMTs is to calculate energy deposition from photons produced in Argon scintillation. Photomultipliers will also aid in distinguishing neutrinos from the cosmic ray background. This summer, a 8-inch R5912 PMT was tested. The difference between the Nevis and the MicroBooNE PMT is a lack of a UV wavelength shifter to shift liquid argon scintillation light into the observable spectrum. The Nevis PMT is also able to transmit signal and high voltage (HV) down separate cables. The R5912 PMT gain was studied.

The overall amplification factor, or gain, depends on the number of dynodes, or electron accelerating stages, inside the phototube. The gain, G, of a PMT is defined as the ratio of secondary,N_s to primary,N_p electrons ejected from the final dynode and photocathode repectively,

$$G = \frac{N_s}{N_p}.$$

A common way to calculate these parameters is to use a light emitting diode to pulse the PMT and record the voltage signal it produces on an oscilloscope. The R5912 was placed into a light tight box together with a blue light emitting diode (LED). The LED was pulsed at a frequency of 100 Hz from a digital BNC 565 pulser with a step DC voltage at a width of 30 nanoseconds. The voltage was stepped between 1.3 and 1.7 volts. Two methods to calculate gain were used, variation in peak height, and width. The LED photon emission is assumed to be poissonian. Under this assumption, the number of photoelectrons produced will follow a poisson distribution. The variation in peak heights method is presented here. The PMT gain and number of photoelectrons was measured as a function of input voltage and time (at constant voltage).

To calculate the number of primary photoelectrons produced at the cathode, N_p, we measured the mean variation in peak height over one minute, or N =6000 counts, on an oscilloscope. The average peak height, μ_h, and standard deviation,σ_h, are related to the number of primary photoelectrons by,

$$\mu_h = CGN_p,$$
$$\sigma_h = CG\sqrt{N_p},$$

for C some constant. The ratio of mean to standard deviation gives,

$$N_p = \left(\frac{\mu_h}{\sigma_h}\right)^2,$$

with uncertainties,

$$\mu_h \pm \frac{\sigma}{\sqrt{N}},$$
$$\sigma_h \pm \frac{\sigma_h}{\sqrt{2N}},$$
$$N_p \pm \frac{2\mu_h}{\sqrt{N}\sigma_h}\sqrt{1+\frac{\mu_h^2}{2\sigma_h^2}}.$$

To calculate the number of secondary electrons, the PMT signal was integrated over 6000 triggers yielding the

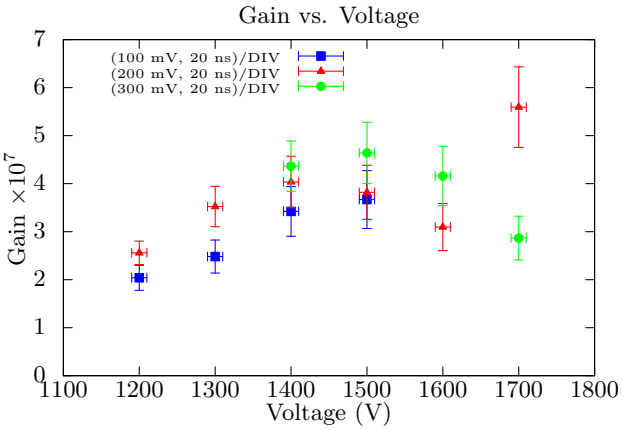

FIG. 4: PMT gain as a function of input voltage at different oscilloscope divisions. Deviation in gain value is observed at constant voltage.

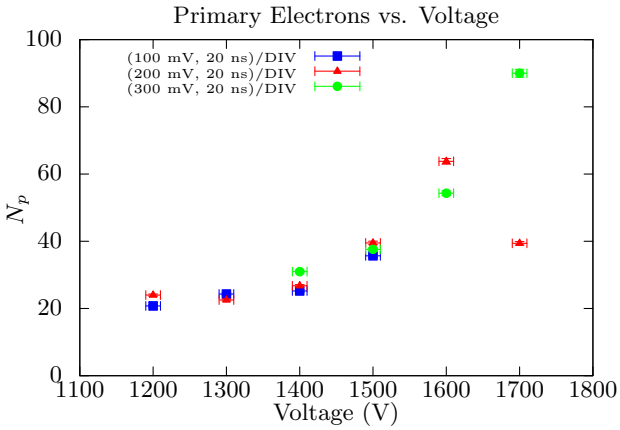

FIG. 5: The number of primary photoelectrons from the cathode as a function of input voltage. We expect the number of electrons liberated from the photocathode to be constant assuming the LED identically pulses the PMT with the same photon energy profile.

charge deposited on the anode. Specifically,

$$N_s = \frac{\int V dt}{eR},$$

with uncertainty,

$$N_s \pm \frac{\Delta\left(\int V dt\right)}{eR},$$

for e the electron charge and $R = 50\ \Omega$ the termination in the oscilloscope. The mean integrated voltage value and standard deviation were used for the charge calculation. The gain is then,

$$G = \frac{\int V dt}{eR}\left(\frac{\sigma_h}{\mu_h}\right)^2,$$

with uncertainty,

$$G \pm \frac{N_s}{N_p}\sqrt{\left(\frac{\Delta N_s}{N_s}\right)^2 + \left(\frac{\Delta N_p}{N_p}\right)^2}.$$

Gain for the R5912 PMT is shown in FIG. 4 plotted at three different oscilloscope window ranges. Only statistical uncertainties are shown. We noticed a deviation in gain value at constant voltage over different oscilloscope ranges. This has been observed before by both Georgia and Leslie. One possible cause of this effect is that upon changing the number of voltage divisions, the scope's precision increases and decreases. Large deviation in gain values from the specification sheet are observed after 1500 volts [13]. After this point the gain drops off suddenly for certain oscilloscope settings. Another method to calculate the PMT gain is necessary to illuminate this issue. FIG. 5 shows the number of primary electron varying significantly as a function of input voltage. At values starting around 1500 V, significant deviations in the photoelectron count are observed, the

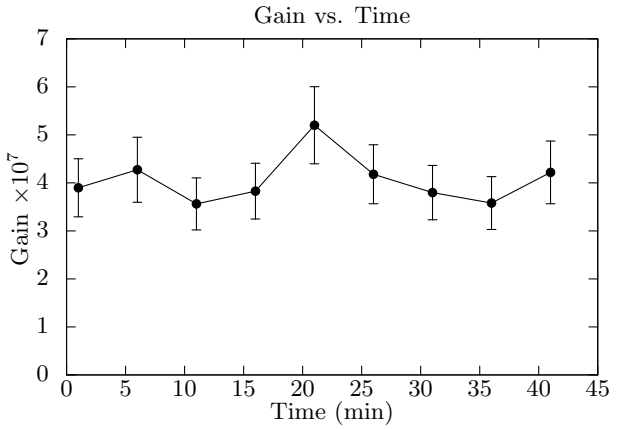

FIG. 6: PMT gain varies in time at constant 1500 V. This is attributed to both a fluctuation between 30 to 50 photoelectrons and 600-800 mV output voltage over 40 minutes.

same value at which the gain deviates from expected. We would expect the same photoelectron count at each voltage. In order to understand the behavior of the PMT as a function of time we measured the output voltage, number of primary electrons and the gain for an input voltage of 1500 V every 5 minutes for 40 minutes. FIG. 6 shows how the gain varies at constant voltage. The gain does not significantly deviate over time. A more accurate assessment of the time dependence of gain would require longer periods of operation. Finally, we incorporated all measurements made in one week from different oscilloscope settings to estimate the systematic uncertainties. In FIG. 7, red triangle data points show all measurements made. Blue points represent the average gain for each input voltage. The gain value exhibits large deviation in the high input voltages of 1600 and 1700 V. The systematic uncertainties in the gain dominated the statistical

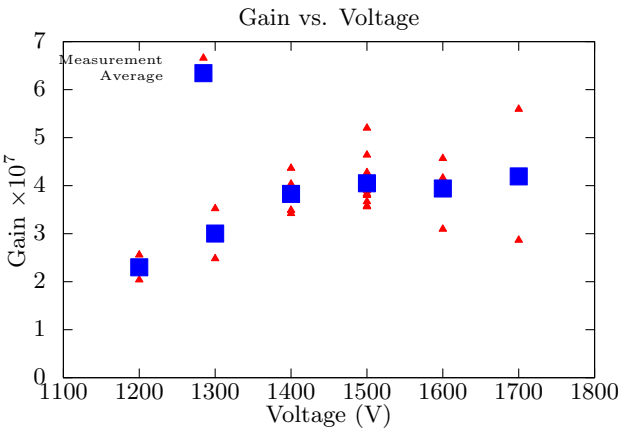

FIG. 7: PMT gain as a function of input voltage with all measurements taken over a period of a week included. The blue square represents an average measurement at constant voltage. The red triangle is a measurement. The systematic uncertainties in the measurement dominated at high voltage.

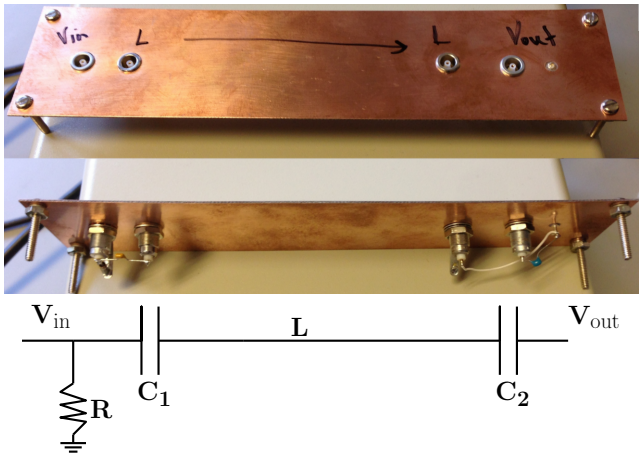

FIG. 8: Circuit used at Nevis to test the Bo splitter capacitance. $V_{\rm in}$ is a step function from the pulser, $V_{\rm out}$ is the signal output to the shaper. The values of C_1, C_2, and L are varied. $R = 50\,\Omega$

uncertainty at high input voltages. Further tests at high voltage are necessary.

While this specific photomultipler tube will not be used in the MicroBooNE detector, it will be used to test the data acquisition system for MicroBooNE at Nevis. A knowledge of the PMT response over input voltage, and time are essential in calibrating the electronics hardware.

B. Splitter Reflection

A current effort to test MicroBooNE's optical electronics setup is called Bo. Bo is a liquid argon training ground for the MicroBooNE optical system including cryogenic photomultipliers, high voltage system, cables and splitters, read out electronics and much more [16]. In Bo, an issue has arisen in the phototube splitters which are similar to those to be used in MicroBooNE.

The output signal from a single PMT in MicroBooNE will have to exit on the same cable that transports high voltage to the cathode. Isolating the PMT signal from the high voltage requires placing a blocking capacitor, or splitter, along the cable which connects the PMT to the shaper board. A portion of the signal that reaches the splitter will be reflected back along the cable. These reflections cause secondary voltage peaks to be produced in the splitter output, with time-delays relative to the original signal on the order of the signal travel-time across the wire. This secondary interference is analyzed by the shaper along with the original signal and can cause distortions in the the final output. A clean shaper signal is important to digitization by the front end module analog to digital converters. Reflection is observed in the shaper output if one of the two criterion are satisfied.

1. The secondary pulses due to reflections have large enough amplitude. The amplitude of the reflections depends on the value of the capacitance acting as a splitter. Larger capacitors will allow a smaller fraction of the signal from reflecting.

2. The frequency at which these reflections occur is low. This is dependent on the length of the cable. The shaper integrates over a wide enough time window such that fast oscillations in the splitter output are smoothed out and do not influence the shaped signal.

Bill Sippach, an electronics engineer at Nevis Labs, simulated the splitter in SPICE, an analog electronic circuit simulator. He found that for a $R = 50\ \Omega$ impedance coaxial cable in series with the blocking capacitor C the 'ringing' should *not* occur in the shaper output as long as the time constant of the circuit is much larger than the travel time of the signal down the wire,

$$\tau = RC \gg \tau_{\rm travel} = \frac{\rm L}{v_{\rm signal}},$$

for L the length of the cable and $v_{\rm signal} = 1\,{\rm foot}/1.5\,{\rm ns}$ the signal speed. Bill's simulation showed that the time constant of the cable and capacitor should be roughly 3-5 times larger. We simulated the PMT signal output and splitter at Nevis using a simple circuit shown in FIG. 8. The first portion of the circuit simulates the PMT output, a few tens of nanosecond exponentially decaying signal. The signal is fed by 100 μs-wide step potential from a pulser box. The second capacitor, C_2 acts as the splitter. The length of cable connecting the simulated PMT signal and the splitter can be varied. The output is then fed to the signal shaper.

We tested the shaper output of this circuit for different cable lengths and splitter capacitances. Our initial test was for a short cable $L = 4$ m, and long cable $L = 20$ m, C_1 =5 pF, C_2 = 1 nF shown in FIG. 9. The short

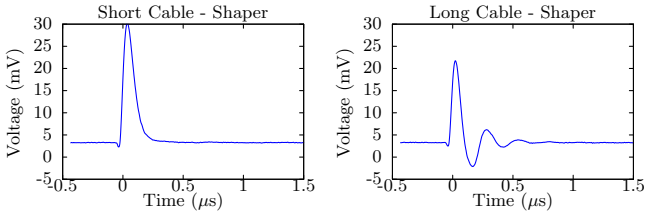

FIG. 9: Shaper output for short cable of length L = 4 m, $C_2 = 1$ nF and for long cable of L = 20 m. Significant ringing is observed in the shaper output of the long cable. The short and long cable input to the shaper resembles the left hand column in FIG. 10. In this test, the reflection in the long cable is 10 times larger in amplitude than in FIG. 10.

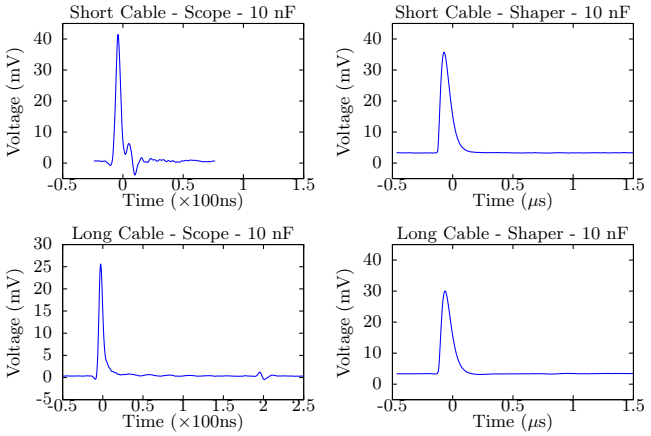

FIG. 10: The left column depicts raw shaper input from the splitter. The right column is shaper output. The splitter capacitance is increased to $C_2 = 10$ nF. No ringing is observed in the long cable despite the low frequency reflection at ~ 200 ns. This is because of a decrease in amplitude from previous FIG. 9. The short cable is presented as an example raw splitter output on the oscilloscope before shaping. The shaper takes this signal as input.

cable sees lots of reflection but because of the shapers long integration time the shaper output is clean and no ringing is observed. The long cable shows ringing in the shaper output, the dip in voltage after the rise, because for this circuit has time constant$\tau = 50$ ns and the signals $\tau_{\text{travel}} = 100$ ns. The ringing comes much later in time with respect to the short cable which is amplified by the shaper.

We then replaced the splitter capacitor with $C_2 = 10$ nF. The effect is shown in FIG. 10. The ringing in the oscilloscope output decreased in amplitude and was no longer found in the shaper output as expected by Bill's simulations since $\tau = 500$ ns. We then replaced the length of the cable with a the same length and electronic specifications as the Bo cable. The length increased from L=20 m to L=30m. The results are shown in FIG. 11. We saw no ringing in the shaper output for the long cable since $\tau_{\text{travel}} = 150$ ns is still much less than $\tau = 500$ ns. With these specifications we expected to see ringing

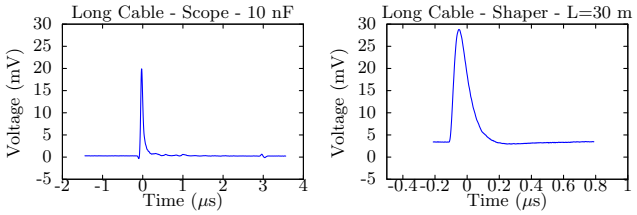

FIG. 11: The length of cable was increased to the same length used in Bo, L=30. Reflection is seen in the oscilloscope output at the 300 ns mark. No ringing is produced in the shaper output as expected.

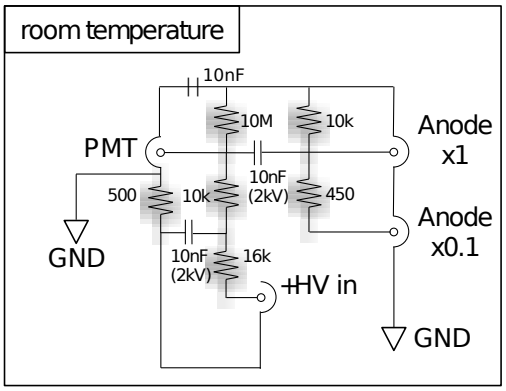

FIG. 12: Circuit schematic for the Bo splitter. 10 nF capacitors channel the high voltage input to the PMT and the central capacitor allows signal to pass through

in the shaper output as the Bo splitter was simulated as best as possible.

In situations in which the time-constant for the circuit is several times larger than that for reflections in the wire, ringing does not present itself. Ringing in the shaper does not appear even if reflections in the splitter output are still present (as seen in FIG. 10, where a small reflection signal can be seen). However, our test for a splitting capacitance of 10 nF and a cable length of 30m which shows no ringing does not agree with the measurements from Bo. For the same parameters, ringing is observed.

We then received the Bo splitter from Fermilab. The circuit diagram is shown in FIG. 12. Upon inspection with Bill we deduced that the capacitor which acts as the splitter in this circuit is the one connecting the PMT input/output directly to the "Anode x1" output. The splitting capacitance is a 10 nF capacitor creating a 500 ns time-constant for RC (as mentioned above). This would be sufficiently larger than the 150 ns travel-time for the signal in the long wire, and would mean *no* ringing in the shaper output. There are however two reasons why this description is not correct.

1. The capacitor in the top left of the circuit diagram, connecting the ground of the output anodes and the ground of the PMT can be thought of as in series

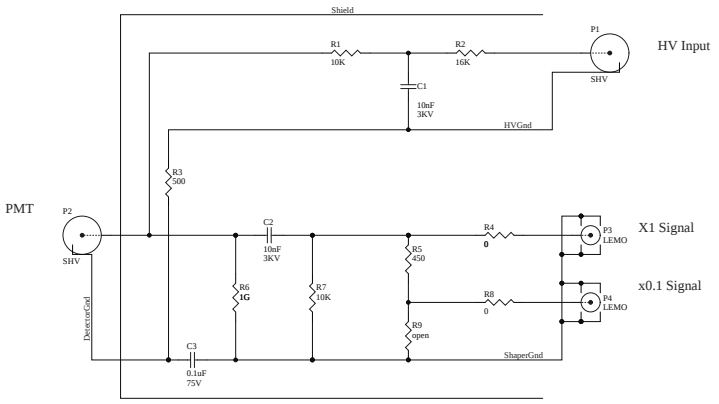

FIG. 13: PMT high voltage splitter for the MicroBooNE detector.

with the main splitter capacitor. This means that overall we have a reduction in effective capacitance. Because the two capacitors are identical the overall capacitance goes down by a factor of two.

2. From the specification sheet, the 10nF capacitor is rated at 3kV (even though the diagram indicates 2kV). When the applied voltage is at the same order of magnitude as that for which the capacitor is rated, the effective capacitance decreases. This happens because the high voltage biases the dielectric in the capacitor, reducing the capacitance. The capacitors used in the Bo splitter are Z5U and at an applied voltage of 1.4 kV, the same voltage which used for the PMT. For a 3 kV rated capacitor this induces a further reduction of the capacitance of around $\sim 12\%$. One can also find the more detailed spec sheets for the individual capacitors.

FIG. 13 shows a diagram for the MicroBooNE splitters that are now being manufactured. The overall layout of the circuit is identical to that of Bo. First the second capacitor, $C_2 = 10$ nF can be thought of as in series with the splitting capacitor now at $C_3 = 100$ nF. This makes the equivalent capacitance lower. Furthermore, even though the splitting capacitor is rated for 3 kV and will have a similar voltage of 1.4 kV applied to it, it is a different type of capacitor: Z7R [14], which loses less capacitance as high voltage is applied. The drop in capacitance is only expected to be roughly $\sim 5\%$. With a crude estimation, we can predict the 10 nF capacitor to result in an actual capacitance of 10 nF $\rightarrow$ 9.5 nF $\rightarrow$ $C_{eq} = 1/(1/100 + 1/9.5)) = 8.67$ nF. This corresponds to a time-constant of 433 ns. This is not quite 3 times as much as the signal travel-time in the wire. Ideally, Bill Sippach mentioned that the RC time-constant should be at least 3, and preferably 5 times larger than that of the cable. Currently the MicroBooNE splitter still sees reflections. The splitter capacitance in the MicroBooNE circuit is to be doubled in value according to [15] as a result of these tests.

IV. LARSOFT ANALYSIS

A. LArSoft Framework

LArSoft, or Liquid Argon Software, is an event generation, simulation, and reconstruction package for liquid argon based particle detectors built on the ART framework. The ART event processing framework coordinates event processing via modules such analysis and event reconstruction, separating the algorithms from raw data. Together with LArSoft specific GEANT4, GEometry ANd Tracking, simulation code, LArSoft is a playground to test the liquid argon time projection chamber based on monte-carlo particle interactions. The essential steps in the monte-carloing of MicroBooNE are event generation, whole detector simulation; particle simulation, reconstruction, identification; and event reconstruction.

An important component of LArSoft is GENIE, Generates Events for Neutrino Interaction Experiments. GENIE takes neutrino information such as 4-momentum, flavor, and interaction-medium and simulates neutrino interactions in all parts of a detector based on geometry. GENIE is the primary neutrino-nucleus interaction simulator which is then passed on to GEANT4 to be propagated. With "flux-files" the user can control a wealth of initial neutrino physics information, mirroring the current neutrino beam specifications such as the Fermilab Booster. The MicroBooNE detector is simulated in GEANT4, a physics package to simulate the passage of particles through matter. GEANT4 models the large scale detector objects such as the cryostat, TPC, optical electronics and their response to particle interactions in the liquid argon. Particle simulation is also processed by GEANT4, including drifting ionization charge to the TPC wireplanes and liquid argon scintillation captured by photomultiplier tubes

After a simulated particle has interacted inside MicroBooNE, a simulated response on the wireplanes and photomultipliers occurs. From the simulated detector response, a reconstruction chain is implemented to identify important event information. Information such as energy deposition, particle track length, vertex, and final state topology are used to reconstruct the true particle information such as particle ID, track, and energy. This information is critical to ultimately reconstructing neutrino interactions in MicroBooNE. To execute particle reconstruction, a chain of algorithms has been devised [16]. The first step in the chain is calibrating raw data such as signals on the TPC wire planes as a function of time. The signal vs. time information is reconstructed above a certain threshold indicating true energy deposition has occurred. This information is called a *hit*. Next, a *cluster* finding algorithm groups the hits which as related to one another spatially and temporally. So far the reconstructed information is only two dimensional. Two dimensional reconstruction is unable to determine track information including distance of interaction vertex and track from a wire. This information is critical to energy

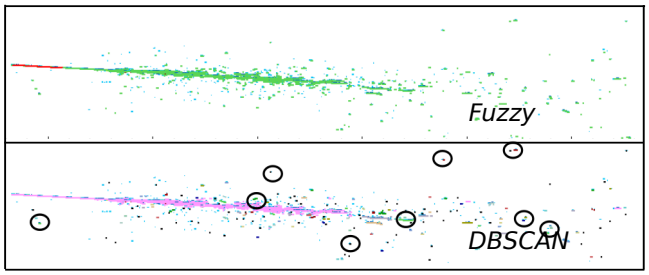

FIG. 14: Example of clustering algorithm on single electron events generated in the center of the MicroBooNE detector. The top panel is Fuzzy cluster and the bottom DBSCAN. DBSCAN contains many small clusters, all different colors, despite the hits being generated from the same electron. A few of the clusters are circled.

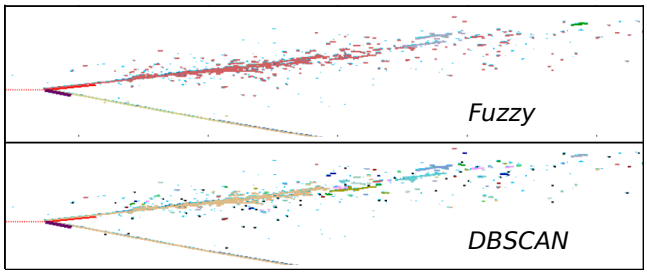

FIG. 15: Example of clustering algorithm on $\nu_e + Ar \rightarrow 1e^- + 1p$ charged current interactions. The top panel is fuzzy cluster and the bottom is DBSCAN. The top shower is an electron shower and the bottom track is the proton. Fuzzy clustering clusters these two object separate, indicated by the two different red and tan colors. DBSCAN does not.

reconstruction as electron recombination between ionization location and wire plane, hindering energy deposition according to Birk [11]. Three dimensional reconstruction is carried out by *track* finding algorithms. These algorithms utilizing timing and hit locations on TPC wires over the three views to build a track. The alternate case is *shower* reconstruction which analyzes $\gamma \rightarrow e^+e^-$ electromagnetic showers resulting from pair producing photons. Once the tracks or showers have been identified a *vertex* finding algorithm locates tracks originating at a common location. The complete three and two dimensional information is stored in an *event* module. From reconstructed final state topologies, information about incoming particles can be reconstructed.

The philosophy behind LArSoft is that code it to be shared between all experiments and written for a broad liquid argon community. The code is shared between a number of experiments such as ArgoNueT, and LBNE. LArSoft is an important tool to study particle interactions with liquid argon before the experiment is completed.

B. Cluster Reconstruction

A signal on a wire can be reconstructed typically using a gaussian fitting algorithm called FFTHit or GausHitFinder. The hit information can be used by a variety of cluster finding algorithms to group them according to some specified criterion. Two mainstream clustering algorithms are DBSCAN and Fuzzy clustering. This summer I studied current clustering algorithms against a specific final state of 1 electron and 1 proton topologies from a charged current interaction inside the detector. I calibrated the data against single electron showers. The event displays for electron and neutrino interactions are shown in FIGs. 14 and 15.

DBSCAN is a density based clustering algorithm proposed by M. Ester et al. in 1996 [12]. The main idea behind the algorithm is for each hit in a cluster the neighborhood of radius epsilon in time and distance has to contain at least a minimum number of other hits. DBSCAN uses a distance function to determine these parameters. With a minimum number of hits and epsilon input, a collection of hits can be scanned to create a cluster. Together with a line finding algorithm, DBSCAN is exceptional at identifying straight track like clusters which 3D reconstruction algorithms capitalize on. Fuzzy clustering is different. Unlike DBSCAN, Fuzzy cluster assigns only "degrees of belonging" to a hit to map clusters. A hit initially belongs to all clusters until the algorithm determines its membership level to a specific cluster after minimizing some objective function. Fuzzy clustering is powerful at clustering particle showers. The algorithm is especially powerful at clustering separately one non-showing particle from another if they share the same interaction vertex as in FIG. 15.

To study the clustering algorithms I generated 100 single electron events at 1.5 GeV and 5000 charged current events filtering for $1e^- + 1p$ final states. I wrote a LArSoft analysis module called `MCHitter` to calculate the *purity* and *efficiency* of reconstructed clusters. Using the `BackTracking` algorithms in LArSoft the module executes the following:

1. Identify all reconstructed clusters on this three wire planes and use the backtracker object to map the reconstructed hits to the clusters.
2. Identify each reconstructed hit and store the truth level information for the particle which contributing ionization energy.
3. Map all true particles to their hits and calculate the purity and efficiency of each cluster defined below.

Cluster purity is defined as,

$$\text{Purity} = \frac{\#\text{ of hits from trackID in cluster}}{\text{total }\#\text{ of hits in cluster}}.$$

As an example, consider a collection of 50 hits produced from two particle tracks, an electron and a charged pion grouped into one cluster. At truth level the electron produced 15 of the hits while the pion produced 35. The

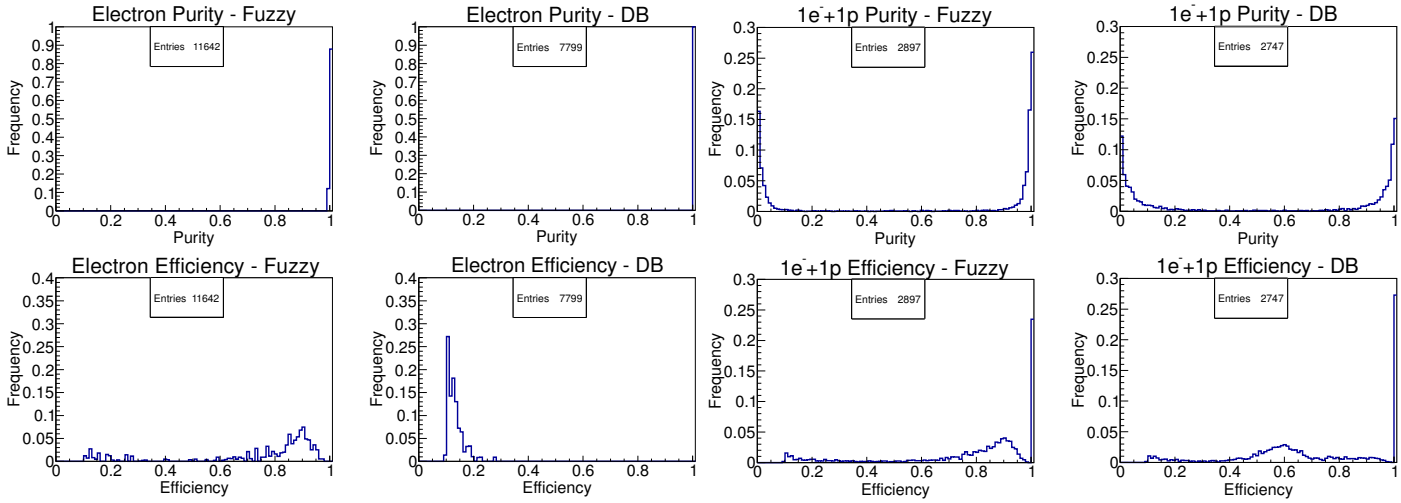

FIG. 16: Single electron events. Fuzzy clustering applied on the left and DBSCAN on the right.

FIG. 17: $1e^- + 1p$ final states. Fuzzy clustering applied on the left and DBSCAN on the right.

purity of the electron in this cluster is $15/50 = 0.3$. The purity of the pion in this cluster is $35/50 = 0.7$. Purity is a measure of how much a single cluster is composed of a true particle. If the purity value is less than 1 the clustering algorithm failed to group the true particle hits separate from one another. The reconstructed quantity of the total number of hits in the cluster and the numerator is extracted from monte-carlo truth information.

Cluster efficiency is defined as,

$$\text{Efficiency} = \frac{\#\text{ of hits from trackID in cluster}}{\text{total }\#\text{ of hits for that trackID}}.$$

Consider the previous example except the charged pion produced a collection of hits at another location in the detector such that the total number of hits produced by the pion is 100. In the first cluster the pion produced 35 hits and in the second cluster 65. The pion efficiency in cluster one is $35/100 = 0.35$ and $65/100 = 0.65$ in the second. Efficiency is a measure of how many of all particle hits lie in a specific cluster. If efficiency is less than unity, the clustering algorithm did not group all the particle hits into a single cluster. The only reconstructed parameter is the grouping of hits into a cluster, all other information is truth level.

For both single electrons and $1e^- + 1p$ final states, clusters with extremely low efficiency made the results difficult to discern between the two algorithms. Therefore, I have cut on efficiencies greater than 10% since these clusters containing only one or two particle hits are are not representative of the cluster group as a whole.

The first group is single electron events. The results are shown in FIG. 16. Each entry corresponds to a cluster. Frequency is the fraction of all clusters analyzed. As expected, the DBSCAN and Fuzzy clustering algorithms produced nearly identical purity plots since only single electrons were generated. In the efficiency graphs on the second row of FIG. 16 the efficiency plots have very different features. Fuzzy clustering grouped the resulting electron shower into larger clusters containing more hits than DBSCAN. This is expected from the event display in FIG. 14. DBSCAN on the other hand, produced much less efficient clusters. These clusters did not contain much of the large electron shower and have lower efficiencies compared to Fuzzy cluster. From this calibration sample both Fuzzy cluster and DBSCAN suffer from low efficiency clusters containing only 1 or two hits verified by the event displays. Fuzzy clustering has a qualitatively better efficiency spectrum. The second group of events is the one electron and one proton final states showing in FIG. 17. The goal of this study was to determine whether fuzzy clustering on average could identity the electron shower from the proton track at the interaction vertex. Distinguishing the two true tracks at the two dimensional level would allow three dimensional tracking algorithms to capitalize on their separation. The purity plots between the two algorithms in the top pane show that Fuzzy cluster is more likely to cluster the two tracks separately. The number of high purity clusters for fuzzy cluster is greater than that of DBSCAN for the same data set. As shown in FIG. 15 DBSCAN is unable to distinguish the two true particle tracks leading to low purity clusters. The Fuzzy clustering algorithm does not group the electron and proton hits separately 100% of the time. This is why the distribution of purities is not unity. The efficiency plots reveal something more striking. Of the clusters studied, Fuzzy clustering was able to group the entirety of true particle tracks into one cluster much better than DBSCAN. In the bottom pane of FIG. 17 the small peak shifts left between DBSCAN and Fuzzy cluster.

Overall Fuzzy cluster was found to better cluster showering particles than DBSCAN. Not shown here, a small sample of 100 1.5 GeV muons was studied. Muons are minimally ionizing particles with very straight tracks

passing through the length of the detector. It was found that while fuzzy cluster was unable to produce completely pure clusters, it was much more effective at containing most of the muon hits along its trajectory, nearly tripling efficiency over DBSCAN.

Cluster reconstruction is an important step in the reconstruction chain. Current clustering algorithms are able to provide physics based hit clustering to tracking finding algorithms later in the chain. Fuzzy clustering shows improved purity and efficiency distributions for filtered $1e^- + 1p$ filtered final states. Both fuzzy clustering and DBSCAN suffer from low efficiency clusters dominating from showering particles.

C. Energy Reconstruction

One of the primary goals of any reconstruction code is to determine the energy of incoming particles in the detector. Typically, calorimetry analysis uses 3D tracks to reconstruct particle energy. Complete event energy reconstruction is currently in its infancy. Instead I studied the visible energy deposition on the TPC wireplanes. The reconstructed hits provided this information. I wrote an analysis module called `MCCounter` to study the energy deposition for the collection plane. I generated 1000 single electrons at 1 GeV and and 1000 electrons between a uniform range of 0.5-5 GeV in LArSoft. Electrons were chosen because of their ability to produce showers in the detector, depositing a large amount of ionization charge over a broad area. I then reconstructed the hits and clusters with FFTHit and Fuzzy cluster.

FIG. 18 shows the number of reconstructed clusters for the two samples. The mean number of reconstructed clusters had similar distributions with the 1 GeV having a higher mean. In the 0.5-5.0 GeV electron sample the number of reconstructed clusters is energy independent.

Energy deposition on the TPC collection planes is in the form of electrons propagated through the wires. FIG. 20 shows the fraction of *true* energy deposition to true electron energy. This plots are useful at understanding how much of the electrons true energy could, at maximum, be deposited on the wires planes after drift recombination effects. On average about 40-45% of an electrons true energy is deposited on the wires. This is because not all energy depositions are reconstructed. There is a threshold electron count which must be satisfied before the hit is considered for reconstruction. This criterion eliminates a large fraction of energy deposited on the wires leading to an ionization to true energy ratio far from unity. For the 1 GeV electron in the top panel of FIG. 20 the distribution is much narrower than in the bottom pane. The uniform energy electrons have a higher RMS because lower and higher electron will produce different amounts of ionization energy. The higher the incoming electron, the more likely it's hits are above the threshold and counted as energy deposition. The lower energy electrons do not meet this threshold as frequently.

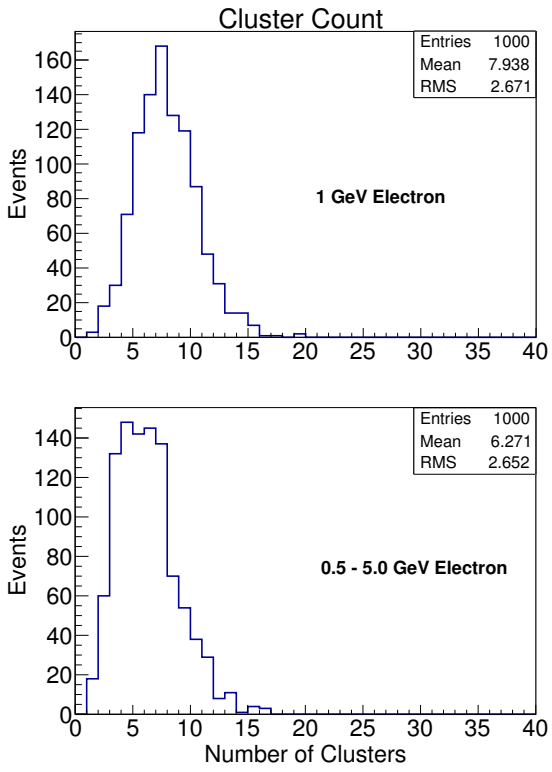

FIG. 18: Number of reconstructed clusters with Fuzzy Clustering algorithm. The top plot is for 1 GeV electrons and the bottom 0.5 - 5.0 GeV. Cluster count appears independent of energy range

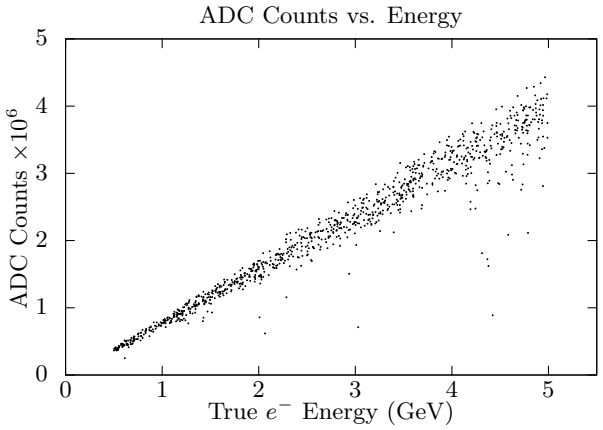

FIG. 19: Reconstructed ADC count on collection plane wires as a function of true electron energy. ADC counts from wires maps linearly with true electron energy.

For the uniform distribution of electron energies, the reconstructed ADC counts are plotted versus true energy in FIG. 19. Reconstructed ADC counts are the analog to digital conversion units specific to the detector electronics. Higher ADC values correspond to more ionization

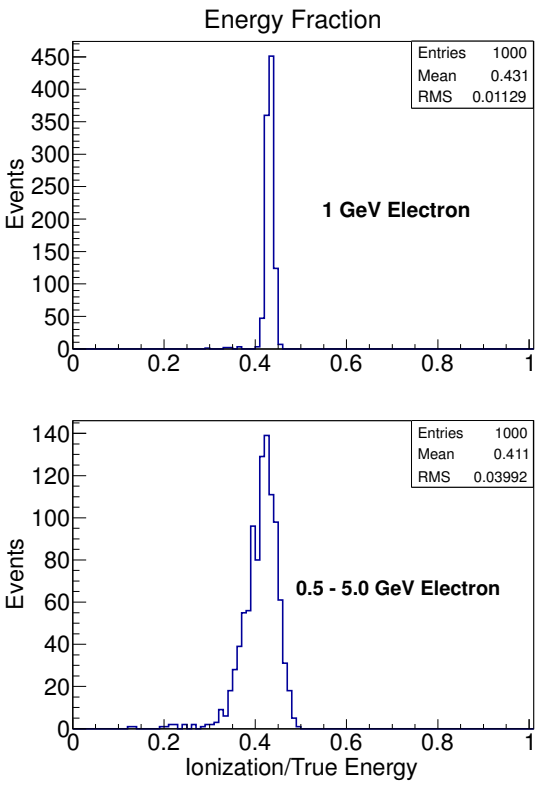

FIG. 20: Energy deposition on TPC collection plane as function of true electron energy. The top plot is for 1 GeV electrons and the bottom 0.5 - 5.0 GeV. Expected energy deposition, or visible energy, is 40% of true electron energy.

electrons deposited in the detector. The scatter plot indicates that for low energy electrons the spread in ADC is less than at higher energies. Despite a few scattered points relationship is roughly linear by eye.

The energy studies done here are important for calibrating the MicroBooNE detector against simulated particle events. Ultimately, reconstruction algorithms *must* become sophisticated enough to distinguish, track, and analyze multiple particle events. Neutrino interactions must be isolated to probe the low energy excess.

V. DATA ACQUISITION

A. Shaper and FEM Set Up

The MicroBooNE detector will employ 30 photomultiplier tubes to record timing for particle interactions inside the detector. A PMT measures incoming photons by generating few nanosecond wide pulse which is sent to the read out electronics. The pulse height and area are correlated to the amount of energy deposited in the phototube. The Nevis group is constructing and calibrating the read out electronics for MicroBooNE. This summer I helped calibrate the shaper and FEM,

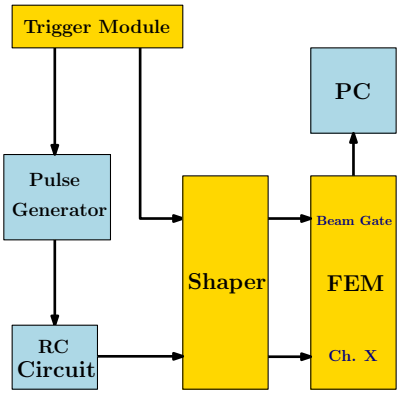

FIG. 21: Shaper and FEM data acquisition set up.

Front End Modules, for the detector. The calibration set up is shown in FIG. 21. A trigger module issues two signals. One pulse is sent to a trigger a pulse generator which outputs a step function to an RC circuit. The voltage amplitude of the pulse generator is stepped between nine levels. The RC circuit produces an narrow PMT-like pulse to the signal shaper. The shaper has 16 channels. The second trigger module pulse triggers the opening of the beam gate, the readout window for data collection. The delay between the beam gate opening and the pulse arrival from the RC circuit can be adjusted. The reason they are not simultaneous is to retrieve information on the ADC pedestal for the first few time samples to estimate the baseline. The purpose of the shaper is to modify the input signal bandwidth to shape the signal before being digitized by the FEM. The shaper effectively smooths high frequency interference and amplifies low frequency interference. The FEM then sends the digitized signal to a PC to be recorded.

The shaper and FEM response is important for energy reconstruction of phototube signals. The shaper and FEM response should be a linear function of input voltage amplitude. Linearity is related to how well one can reconstruct the energy of the PMT pulse. If the response is not linear, it can be corrected by some function.

B. Data Processing

This summer I studied the ADC pedestal, PMT pulse reconstruction, and the shaper-FEM linearity. I wrote a simple pulse reconstruction album with Kazuhiro Terao's Analysis and Decoder package called `pmtbaseline`.

The goal is to correlate the input step function amplitude from the pulser box with the reconstructed charge of the PMT pulse through the electronics system. For each channel on the shaper, a known PMT like pulse is inputted, and reconstructed on a PC after digitization in the FEM. Data was recorded for 10,000 pulses. Estimates for the pedestal height, peak pulse height, start, max amplitude, and end time and charge sum for each pulse were

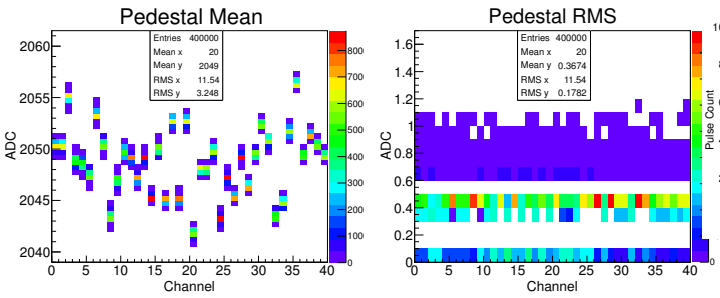

FIG. 22: Pedestal mean and standard deviation for each FEM channel. The spread in ADC mean is roughly 10 ADC count with a primarily 0.5 ADC count variation in one channel.

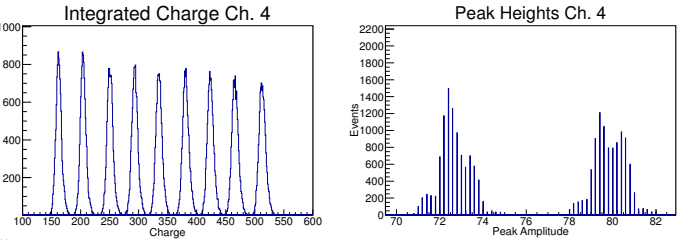

FIG. 23: Left pane plots integrated pulse charge over 9 amplitudes increasing in amplitude by one step. Right pane is zoomed in distribution of two peak height distributions. The peak heights distributions are highly asymmetric.

calculated using the `pmtbaseline` module. This process is repeated for all 16 shaper channels.

C. Results

First, a good understanding of the ADC pedestal is important for pulse reconstruction. The analog to digital converter or ADC measures the total charge sent to it in a specified period of time. When triggered, a gate is opened and the signal is allowed into the device. The charge from the signal is collected on a capacitor, measured and then a digital signal is sent onward, containing the amount of charge collected. A slight complication to this process is that a small quantity of charge is sent to the ADC capacitor whether there is a signal or not. This means that if there was no signal, the ADC will still measure a small quantity of charge called the pedestal. Since this pedestal is always the same during a given run, it can be measured and subtracted. For 10,000 beam gate samples, the first time samples are averaged to estimate the pedestal. The results are plotted in FIG. 22. The ADC pedestal has a mean values between FEM channels of 2049 with a standard deviation of approximately 0.36 ADC counts.

Next, Kazu, Dan, and I used the setup described in FIG. 21 to test the shaper-FEM linearity. For 9 amplitude settings on the pulser box, data was collected over the 16 shaper channels. The raw data was processed with `pmtbaseline`. The integrated charge and pulse amplitude are two estimators of pulse energy. The distributions are plotted in FIG. 23. In the right pane of FIG. 23 the distribution of pulse amplitudes is highly asymmetric due to a digitization effect of the FEM. The digitization splits the otherwise continuous distribution into discrete distributions based on the ADC resolution. Values near the resolution threshold of the ADC either get placed on the left or right of the bit value. A similar effect has been reported on by [17]. Due to this effect it is preferable to separate the distribution into three smaller ones. Three cuts were made on the pulse height distribution because many of the peak height distributions show three peak features. The procedure involves finding the pulse amplitude found in the maximum number of pulses and cutting left and right ± 0.5 in pulse amplitude. The results are shown in the top pane of FIG 24. Cutting on the peak height distribution reveals three corresponding low, middle, and high energy components in the charge distribution: the bottom panel in FIG. 24. For data analysis we choose the middle, blue, distribution as we believe the middle peak heights are the most representative of the true PMT pulse height and therefore the best estimator of the energy value in the charge sum. Scanning the input amplitude between 4 and 12, the middle charge distribution is fit to a gaussian curve and the results for one channel are presented in FIG. 25.

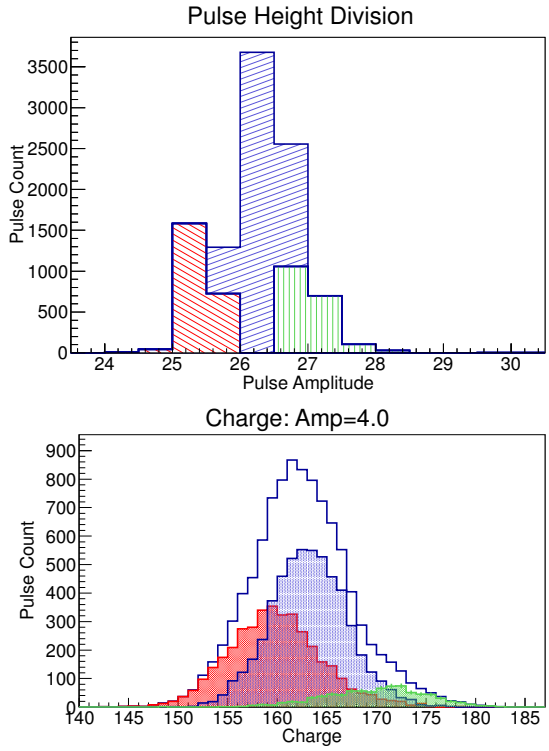

FIG. 24: Cuts on the pulse height distribution in the top pane reveal three distinct Gaussian like charge sums in the bottom pane.

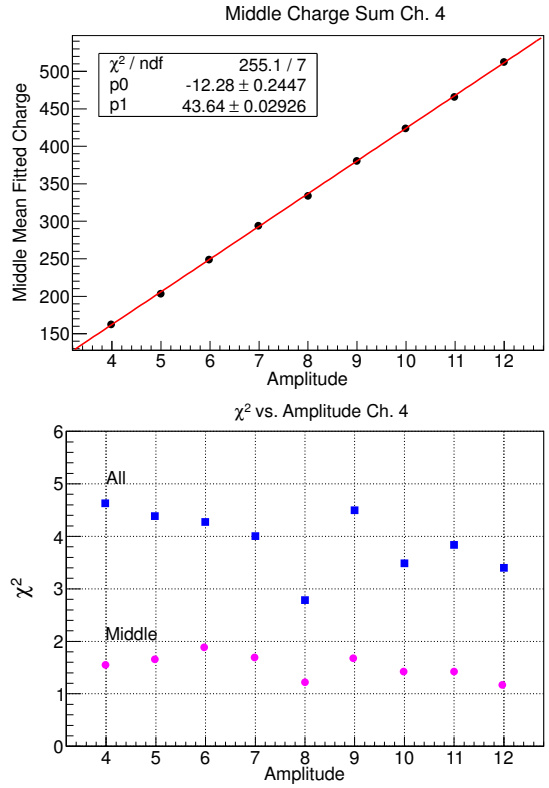

FIG. 25: Linear fit to mean charge from gaussian fit of middle charge distribution as a function of input amplitude from pulser box. The bottom panel is a plot of χ^2 value for each gaussian fit over the amplitude range.

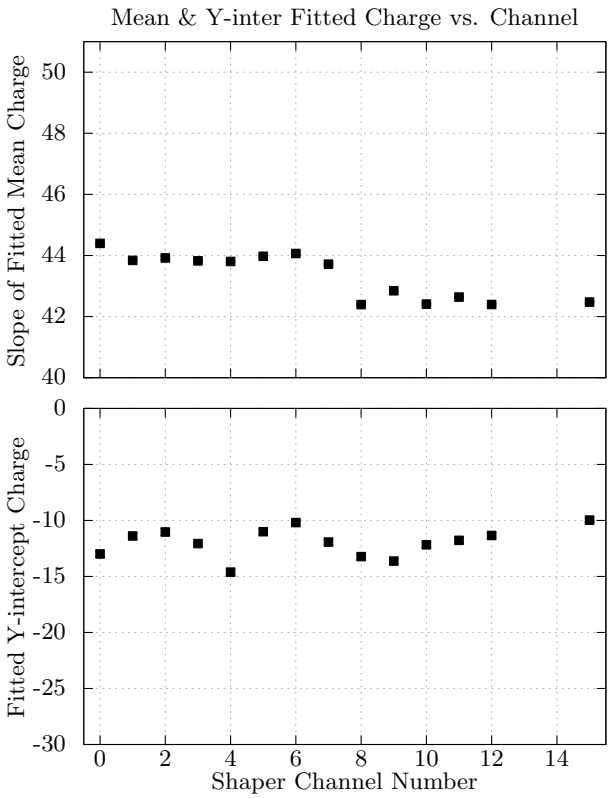

FIG. 26: Fitted Mean and Y-intercept values for the linearity plot in the top panel of FIG. 25. The slope varies between 42 and 46. The non-zero value of the y-intercept values indicated some non-linearity at low amplitudes.

The fitted mean value is plotted against input amplitude. The relationship is linear. The size of the fitted mean error bar is smaller than the size of the dot. Unfortunately the statistical uncertainty in the gaussian fit is extraordinarily small leading to a large χ^2 value on the linear fit. Systematic uncertainties in measurement have not been included. One way to incorporate this is to give each charge integral measurements a default systematic uncertainty. Despite this, the linearity of the shaper and the FEM is good. The bottom panel in FIG. 25 shows the χ^2 goodness of fit value for the gaussian curve of the middle charge distribution. The blue dots are the χ^2 values for a naive gaussian fit to the charge distribution without cuts. Magenta dots are the χ^2 values for the charge distribution with cuts. The cut distribution fits have a much lower χ^2 value over the range of input amplitudes indicating a better fit.

The slope and y-intercept of mean fitted charge versus amplitude is plotted over the 16 shaper channels. Data for channels 13 and 14 have not been collected yet. The data is shown in FIG. 26. The slope varies between 42 and 46 with errors bars smaller than the dot size. This shows the shaper response is the same between each input channel. The fitted y-intercept value is nonzero and perhaps reveals a non-linearity at low input amplitudes. We would expect a zero gaussian mean at zero input amplitude. Further investigation is necessary.

The signal shaper and FEM response is linear in output with pulser amplitude. The next step is to test the rest of the signal shapers for MicroBooNE and expand on the reconstruction algorithms to account for late light produced from Argon scintillation.

Acknowledgments

I would first like to thank Professor Mike Shaveitz for providing the opportunity to gain experience in MicroBooNE project as well as his helpful criticism during weekly presentations. I would also like to thank Professor John Parson for his administrative finesse throughout the summer.

A big thanks to Kazu for teaching me PyROOT and getting me excited about real physics analysis. Your enthusiasm for software has taught me that anything can be programmed.

I am thankful to Georgia Karagiorgi for getting me started with LArSoft analysis. Her exuberance for neutrino physics is inspiring.

Thanks to David Caratelli for allowing me to be his PMT and Bo ringing partner.

I acknowledge the revisions of Douglas Davis.

Finally, thanks to the National Science Foundation for making this summer possible.

[1] Donald H. Perkins, *Introduction to High Energy Physics* (Cambridge University Press, United Kingdom, 2001), 4th ed.

[2] David Griffiths, *Introduction to Elementary Particles* (Wiley-VCH, 2008) 2nd ed.

[3] B.R. Martin, G. Shaw, *Particle Physics* (John Wiley & Sons, United Kingdom, 2008) 3rd ed.

[4] B. Pontecorvo, "Mesonium and Antimesonium" (J. Exptl. Theoret. Phys, U.S.S.R) 33, 549 (1957).

[5] J. Beringer et al. "Particle Data Group", PR D86, 010001 (2012)

[6] B. T. Cleveland et al (1998). "Measurement of the Solar Electron Neutrino Flux with the Homestake Chlorine Detector". Astrophysical Journal 496: 505526

[7] SNO Collaboration, "Direct Evidence for Neutrino Flavor Transformation from Neutral-Current Interactions in the Sudbury Neutrino Observatory" Phys. Rev. Lett. 89, 011301 (2002)

[8] L. Camilleri, "MicroBoone", Nuclear Physics B Proceedings Supplement 00 (2012) 13

[9] B. Flemming, S. Zeller et al. "A Proposal for a New Experiment Using the Booster and NuMI Neutrino Beamlines: MicroBooNE" (2007)

[10] Ben Jones, "Results from the Bo Liquid Argon Scintillation Test Stand at Fermilab" Light Detection In Noble Elements (LIDINE) at Fermilab, May 29th 2013

[11] Birks, J.B. The Theory and Practice of Scintillation Counting. London: Pergamon (1964)

[12] Martin Ester, Hans-Peter Kriegel, Jrg Sander, Xiaowei Xu, "A density-based algorithm for discovering clusters in large spatial databases with noise" (1996)

[13] R5912 Specification Sheet retrieved from http://www.alldatasheet.com/datasheet-pdf/pdf/62744/HAMAMATSU/R5912.html on July 28, 2013.

[14] X7R Specification Sheet retrieved from http://www.avx.com/docs/catalogs/cx7r.pdf on July 28, 2013.

[15] G. Karagiorgi "Bo readout update" - MicroBooNE Document 2700-v1

[16] B. Jones "Flowcart for larsoft reconstruction" - MicroBooNE Document 2572-v1

[17] W. E. Cleland, E.G. Stem "Signal processing considerat ions for liquid ionizat ion calorimeters in a high rate environment" Nucl. Instr. and Meth. in Phys . Res. A338 (1994) 467-497

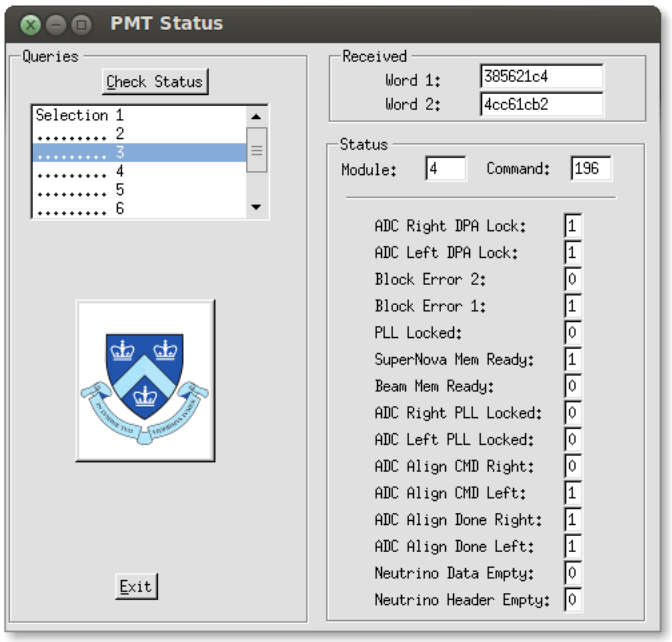

FIG. 27: PMT GUI

Appendix A: Document

Document produced in LaTeXusing REVTeX 4. All graphs were generated by the author in gnuplot using the tikz terminal, and ROOT.

Appendix B: PMT GUI

Toward the end of the summer, I wrote a simple ROOT GUI to interpret the status word output by PMT electronics. WinDriver is software for the PCIE controller on UBELEC in the electronics room used to access the electronics. The GUI takes the two 32-bit status words and prints out the relevant bit information in screen. Currently, Mike Phipps has taken over the project and expanded it to query the TPC crates. A picture of the GUI is shown in FIG. 27. The GUI generates two fake 32-bit words and tests the relevant bits.

Appendix C: Vic's Files

I have a lot of files.

/a/home/houston/vic.genty

- `lardev`
  - `EnergyStudy` - Input a reconstructed root file with spacepoint and track information, output to stdout the reco track coordinates for particle. Cool for plotting in 3D
  - `MCCalo` - Failed attempt at true calorimetry
  - `MCCounter` - True energy studies for hit reconstruction, energy deposition on wireplanes
  - `MCFilter` - Input is ROOT file with clustering algorithm and outputs nothing useful. First attempt at getting information out about hits in clusters
  - `MCFinder` - Input is a ROOT file with clustering algorithm, output to stdout which final states are 1e+1p. Used to look a event display.
  - `MCHitter` - Output is ROOT file with purity and efficiency plots for single electron and proton final states sorted by wireplane. Use with ROOT macro in `~/larscripts`
- `larwork`
  - Lots of LArSoft generated ROOT files listed (mostly) by date. Most have been generated and reconstructed with an outdated LArSoft version so they will become useless.
- `larscripts`
  - `coolplots_MCCounter` - Before I learned PyROOT I used CINT. Takes ROOT files from `MCCounter` and displays the tree contents. Use —readroots.C—.
  - `loops_MCHitter` - Takes ROOT files from `MCHitter` and plots the tree contents. Use `readroots.C` for $1e^- + 1p$ and `readroots_muonselectrons.C` for single electrons and muons.

If deleted: a full backup ($\sim$ 14 GB) can be found in `a/data/morningside/vic.genty/houston`

/a/data/westside/vic.genty

- `0617release`- 5000 CC events generated with GENIE for the 0617 release of LArSoft. There are some muons here too.
- `0625release`- 5000 CC events generated with GENIE for the 0617 release of LArSoft. There are some electrons and muons here too.

/a/data/morningside/vic.genty

- `calo_tests` - Nothing useful.
- `houston` - Back up of home folder.
- `runs` -
  - `nue_cc_uniform` - At one point during the summer, after LArSoft updated, it was terribly hard to generate ν events with GENIE. The program `lar` would eat up gigs and gigs of virtual memory eventually erroring out. These are 100 CC events each I was able to generate and test with the June 25 release of LArSoft.

– `runs` - Single electrons I generated with June 25 release to study energy deposition. 10, 1000, 5000 at mono- and uniformly-energetic electrons produced.